Supporting materials for:

Stable Twisted Conformation Aza-BODIPY NIR-II Fluorescent Nanoparticles with Ultra-large Stokes Shift for Imaging-Guided Phototherapy

Youliang Tian, Huiting Zhou, Quan Cheng, Huiping Dang, Hongyun Qian, Changchang Teng, Kai Xie, Lifeng Yan*

Hefei National Laboratory for Physical Sciences at the Microscale, CAS Key Laboratory of Soft Matter Chemistry, and Department of Chemical Physics, University of Science and Technology of China, Hefei, Jinzairoad 96, 230026, Anhui, China.

Materials and apparatus

4-(N,N-diphenylamino)benzaldehyde, 4-methoxyacetophenone, nitromethane, 1,8-diazabicyclo[5.4.0]undec-7-ene (DBU), diethylamine, ammonium acetate, N,N-diisopropylethylamine, boron (tri) fluoride etherate ($BF_3 \cdot C_2H_5OC_2H_5$), N-bromosuccinimide, N-iodosuccinimide, 1,3-diphenylisobenzofuran (DPBF), methylene blue(MB) was purchased from Aladdin Corporation (China). Methyl thiazolyl tetrazolium (MTT), fluorescein diacetate (FDA), and propidium iodide (PI) were obtained from Sangon Corporation, China. Reactive Oxygen Species Assay Kit was purchased from Beyotime Biotechnology Corporation. All the solvents used in column chromatography come from J&K (China).

^1H NMR and ^{13}C NMR spectra were scanned on Bruker AC 100/400/500 spectrometer with chloroform-d ($CDCl_3$) as solvent. High-resolution mass spectral analysis (HRMS) was performed on Waters XEVO G2 Q-TOF (Waters Corporation) or Atouflex Speed (Bruker Corporation).

UV-Vis absorption spectra were recorded by a UV1700PC (ultraviolet spectrophotometer). The NIR-II fluorescence emission spectra were recorded using an Edinburgh FLS1000 fluorescence spectrophotometer equipped with an 808 nm laser

diode. The temperature variation curve of the micelle was recorded by an Atest thermometer (DT-847UD). Ultrapure water was obtained from a Milli-Q Synthesis System (Millipore, Bedford, MA, USA). The particle sizes and their distributions were detected by a zeta-potential analyzer with dynamic laser light scattering (DLS) by a Malvern Zetasizer Nano ZS90 machine containing a He–Ne laser. The size and morphology of the micelle were measured by transmission electron microscope (TEM, JEM-2100). Fluorescence imaging *in vitro* was carried out by using a fluorescence microscope (IX71, Olympus). The whole-body NIR-II fluorescence imaging was performed by using an *in vivo* NIR-II imaging system. Briefly, an 808 nm diode laser was chosen as exciter and an InGaAs camera (C-Red2) was used to image the small animal models. The thermal imaging of mice was detected by an infrared thermal camera (Fotric 225S, ZXF Laboratorise, LLC).

293T cells from ATCC (American Type Culture Collection) were cultured in Dulbecco's Modified Eagle's medium (DMEM, Hyclone, USA) with 10% fetal bovine serum (FBS, ExCell Bio, Shanghai, China) at 37 ^{o}C with 5% CO_2. 4T1 cancer cells from ATCC (American Type Culture Collection) were cultured in RPMI（1640）with 10% fetal bovine serum (FBS, ExCell Bio, Shanghai, China) under the same condition.

Singlet oxygen trap experiments

The singlet oxygen production capacity of TAB, TAB-2Br, and TAB-2I in DCM was studied using DPBF as a singlet oxygen trap molecule. Methylene blue (MB) was used as the reference compound with a singlet oxygen quantum yield of 0.57 (in DCM). The absorption at 414 of DPBF will decrease gradually after it interacts with singlet oxygen. In the initial stage of the experiment, the absorbance value of DPBF at 414 nm was approximately controlled in the range of 1.5~2.0, the concentration of photosensitizer was controlled in the range of 3~5 uM, and the power density of 635 nm laser was 25 mW/cm^2.

The singlet oxygen quantum yield ($^{\Phi_\Delta}$) of photosensitizer was calculated by the formula below.

$$\Phi_{\Delta} = \Phi_{MB}\frac{k\ \ 1-10^{-A_{635}^{MB}}}{k_{MB}1-10^{-A_{635}}}$$

Φ_{MB} is the singlet oxygen quantum yield of the MB in DCM (0.57), k and k_{MB} are slopes of plots, which represent the absorbance at 414 nm of DPBF in the photosensitizers and MB, respectively. A_{635}^{MB} and A_{635} is the absorbance at the irradiation wavelength (635 nm) of the MB and photosensitizer at the beginning, respectively.

The same processes were also performed by using an 808 nm laser with a power density of 25 mW/cm^2.

Photothermal effect and photothermal conversion efficiency calculation of nanoparticles

First of all, in order to evaluate the photothermal effect of nanoparticles, pure water and 25 μM P-TAB, P-TAB-2Br, and P-TAB-2I nanoparticles were irradiated by 808 nm laser with a power density of 0.8 W/cm^2. The temperature changes were monitored by an Atest thermometer (DT-847UD). Next, we considered the effect of concentration on temperature. Different concentrations of nanoparticles (15 μM, 30 μM, 60 μM) were prepared and irradiated by an 808 nm laser with a power density of 0.8 W/cm^2 for 5 min. Then, the effect of power density on temperature was discussed. P-TAB, P-TAB-2Br, and P-TAB-2I nanoparticles were irradiated by 808 nm laser at different power densities (100 mW/cm^2, 250 mW/cm^2, 400 mW/cm^2, 550 mW/cm^2,700 mW/cm^2, 850 mW/cm^2 and 1000 mW/cm^2). To measure the photothermal conversion efficiency, P-TAB, P-TAB-2Br, and P-TAB-2I (25 μM) were exposed to 808 nm irradiation at 0.8 W/cm^2 for 5 min, and then the solution was cooled down to room temperature. The temperature of the solution was recorded at an interval of 15 s during this process. The photothermal conversion efficiencies (η) were measured according to the reported method [1].

$$\eta = \frac{hs(T_{Max} - T_{Surr}) - Q_{Dis}}{I\left(1-10^{-A_{808}}\right)}$$

h is the heat transfer coefficient; s is the surface area of the container. Q_{Dis}

represents heat dissipated from the laser mediated by the solvent and container. I is the laser power and A is the absorbance at 808 nm.

$$hs = \frac{mC_{water}}{\tau_s}$$

m is the mass of the solution containing the photoactive material, C is the specific heat capacity of the solution (C_{water}= 4.2 J/(g•°C)), and τ_s is the associated time constant.

$$t = -\tau_s In(\theta)$$

θ is a dimensionless parameter, known as the driving force temperature

$$\theta = \frac{T - T_{Surr}}{T_{Max} - T_{Surr}}$$

T_{Max} and T_{Surr} are the maximum steady-state temperature and the environmental temperature, respectively.

Stability exploration of nanoparticles

The resistance to photobleaching of different nanoparticles was measured using a UV-Vis absorption spectrometer. Briefly, the absorption spectra of nanoparticles were recorded after being irradiated for different time (0 min, 5 min, 10 min, 15 min, 20 min) using 808 nm laser with a power density of 1.25 W/cm^2. For the resistance to pH, the nanoparticles with the same concentration (40 μM) were incubated in various pH for 2 h, the absorption spectra were recorded and the fluorescence imaging and photothermal effect in different pH solutions were tested. Analogously, the resistance to H_2O_2 was tested using the same method (H_2O_2: 200 μM). Photothermal stability of nanoparticles (50 μM) was measured by a circle of the heating-cooling process (808nm, 1.25 W/cm^2).

Chicken penetration model assay

Three NPs (100 μM) were filled in a capillary tube (diameter: 0.5 mm). Then, the capillary tube was adhered to a black paper and taken photographs for imaging. The depth of penetration was tested by changing the different thicknesses (0, 1, 2, 3, 4, 5, and 6 mm) of chicken meat and detecting the varied fluorescence intensity of

nanoparticles in a capillary tube.

Tumor model

Female Balb/c mice (5 weeks old, Beijing Vital River Laboratory Animal Technology Co., Ltd.) have cared under protocols approved by the Animal Care and Use Committee in the University of Science and Technology of China.

In order to build the tumor model, mice were subcutaneously injected with 4T1 cells (about 10^6 per tumor) on the right side for imaging assay, or both sides on the back for *in vivo* phototherapy effect. The mice were further treated when the volume of the tumor reaches about 120 $mm^{3.}$

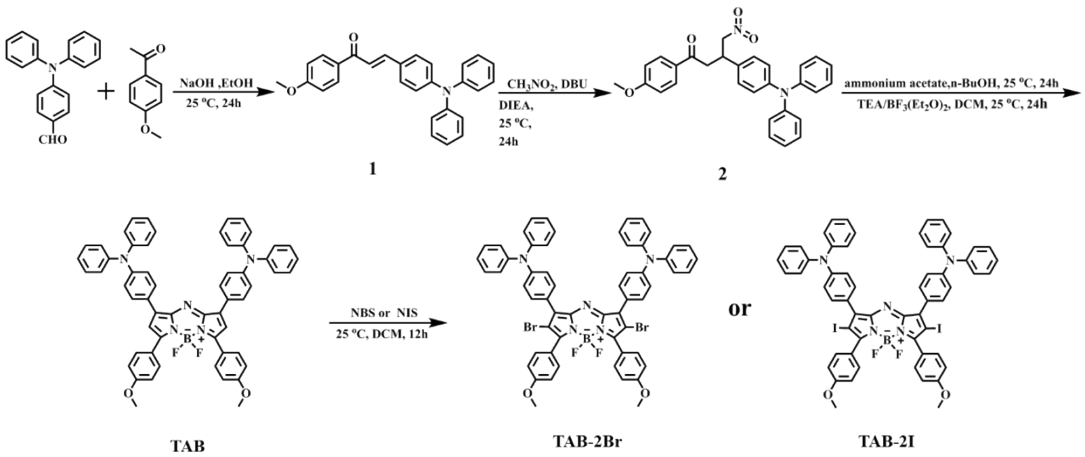

Figure S1. The synthetic route of TABs.

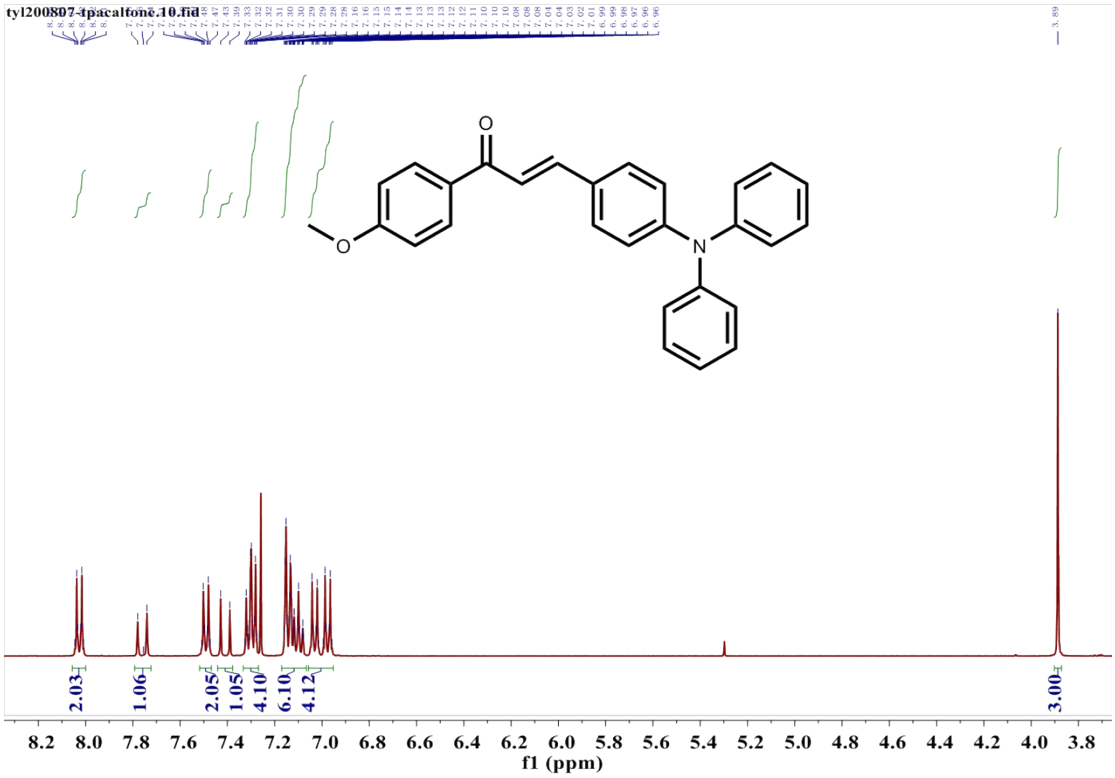

Figure S2. ^{1}H NMR spectrum of compound 1 in $CDCl_3$.

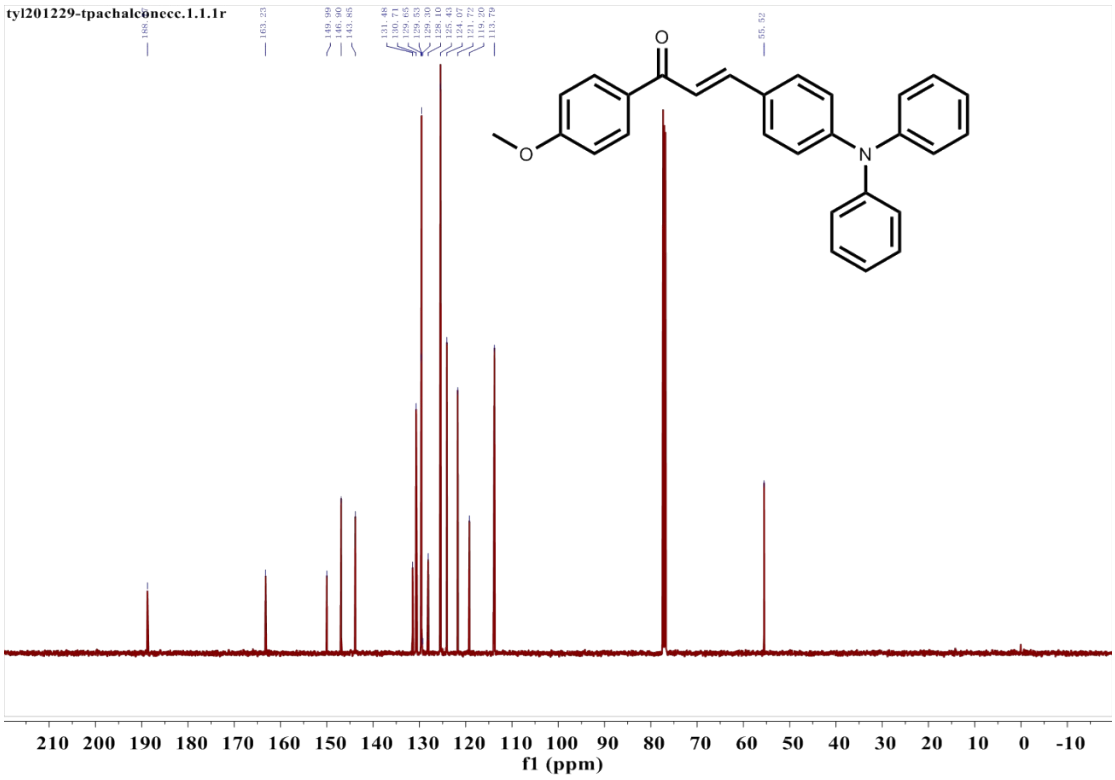

Figure S3. ^{13}C NMR spectrum of compound 1 in $CDCl_3$.

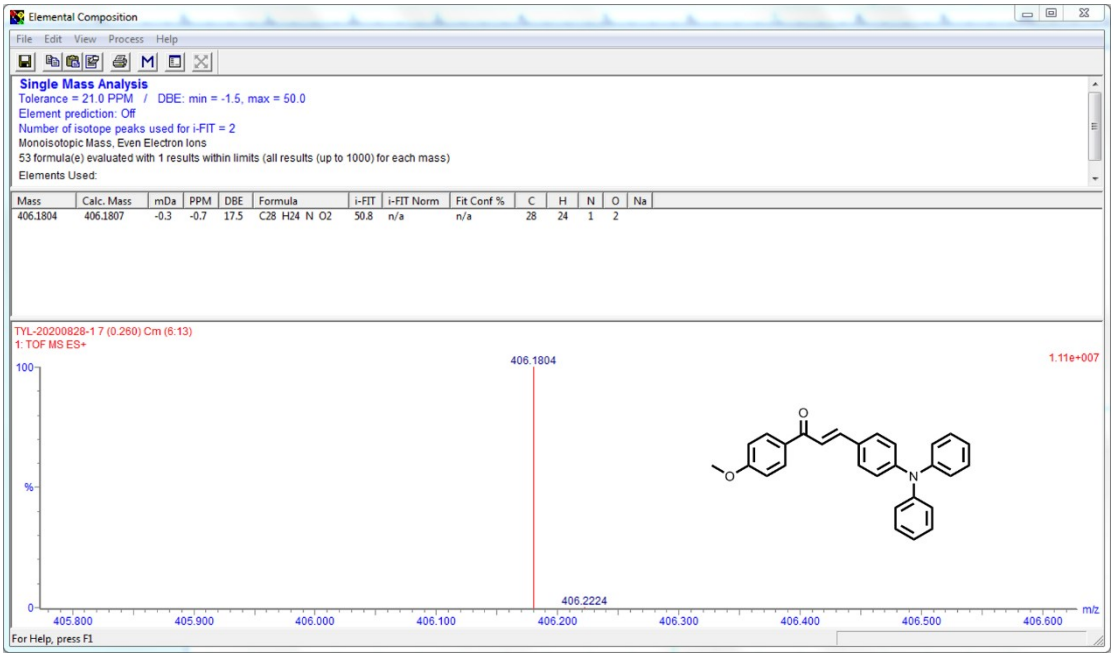

Figure S4. HRMS spectrum of compound 1.

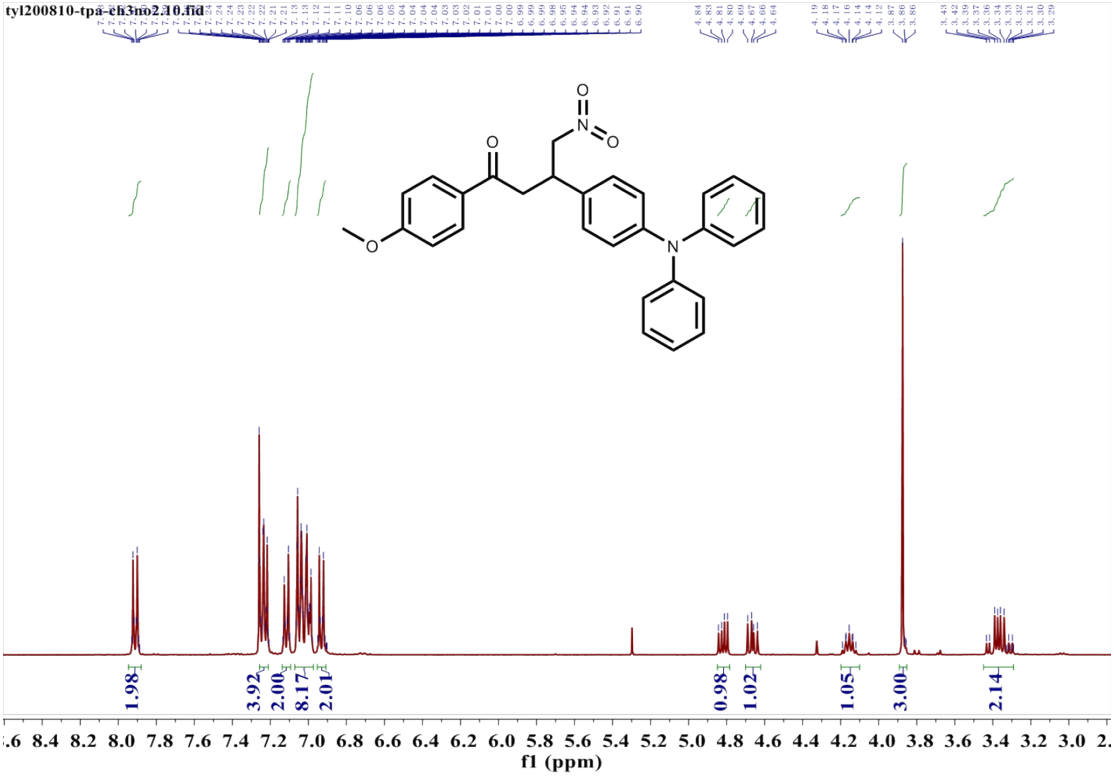

Figure S5. ^{1}H NMR spectrum of compound 2 in $CDCl_3$.

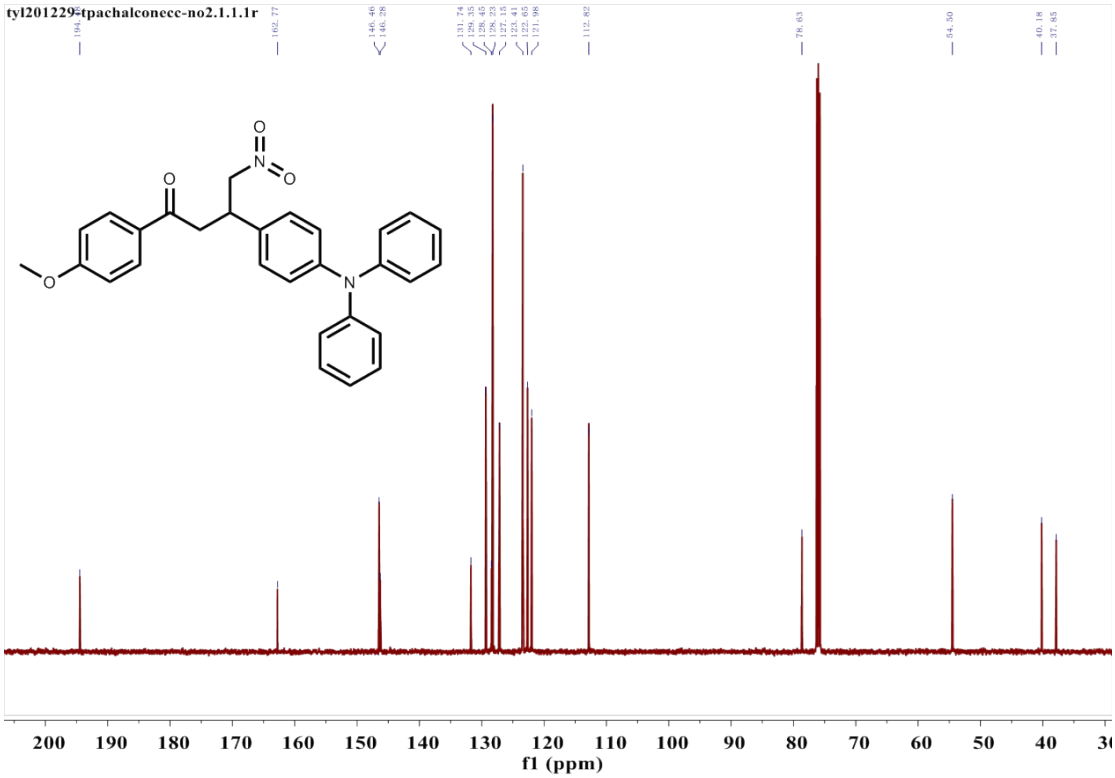

Figure S6. ^{13}C NMR spectrum of compound 2 in $CDCl_3$.

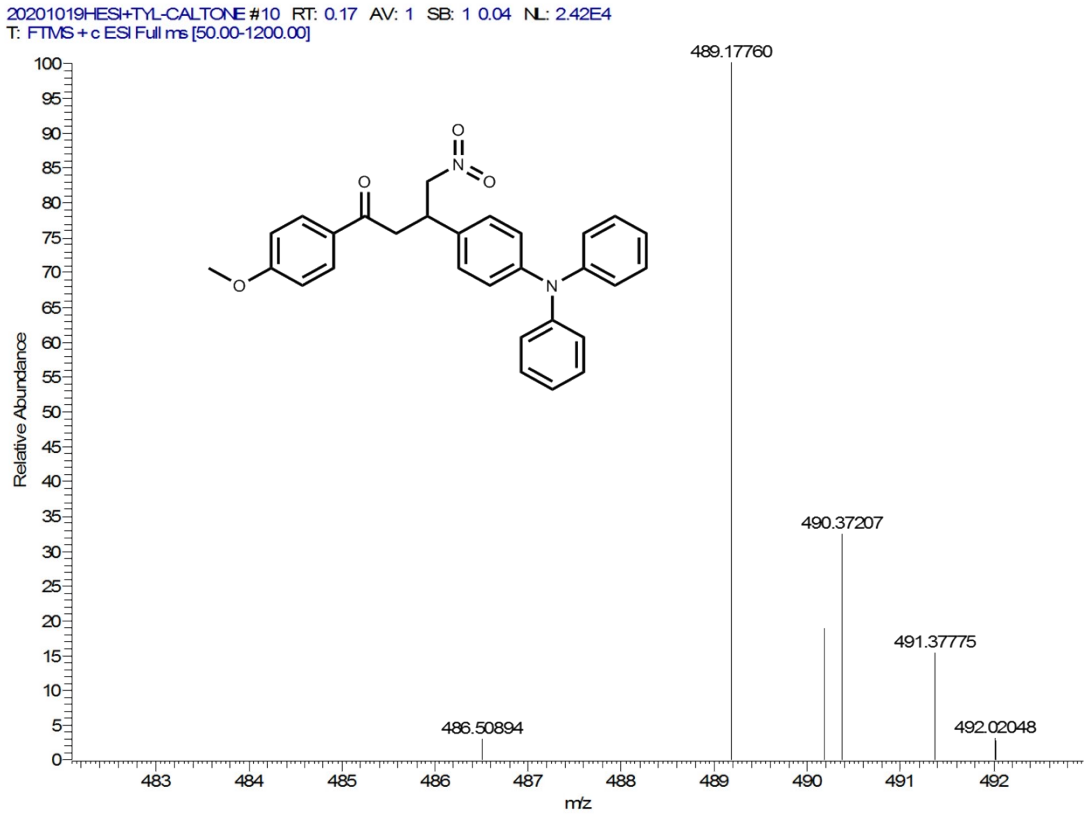

Figure S7. HRMS spectrum of compound 2.

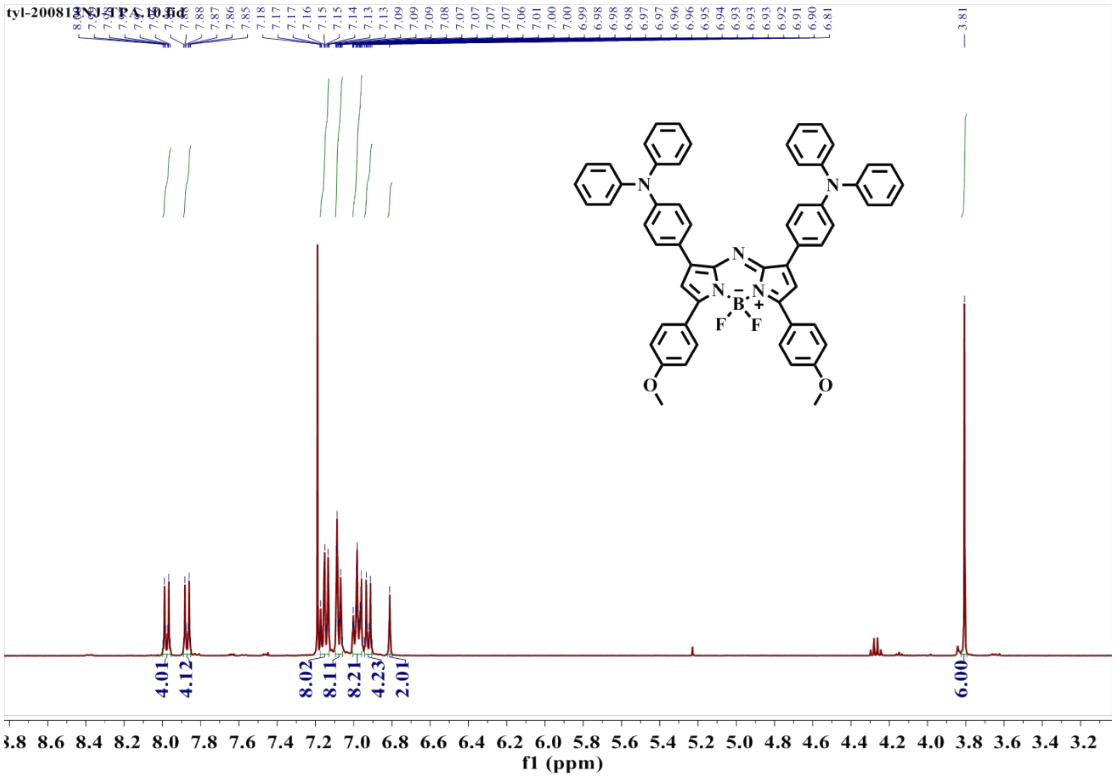

Figure S8. ^{1}H NMR spectrum of TAB in $CDCl_3$.

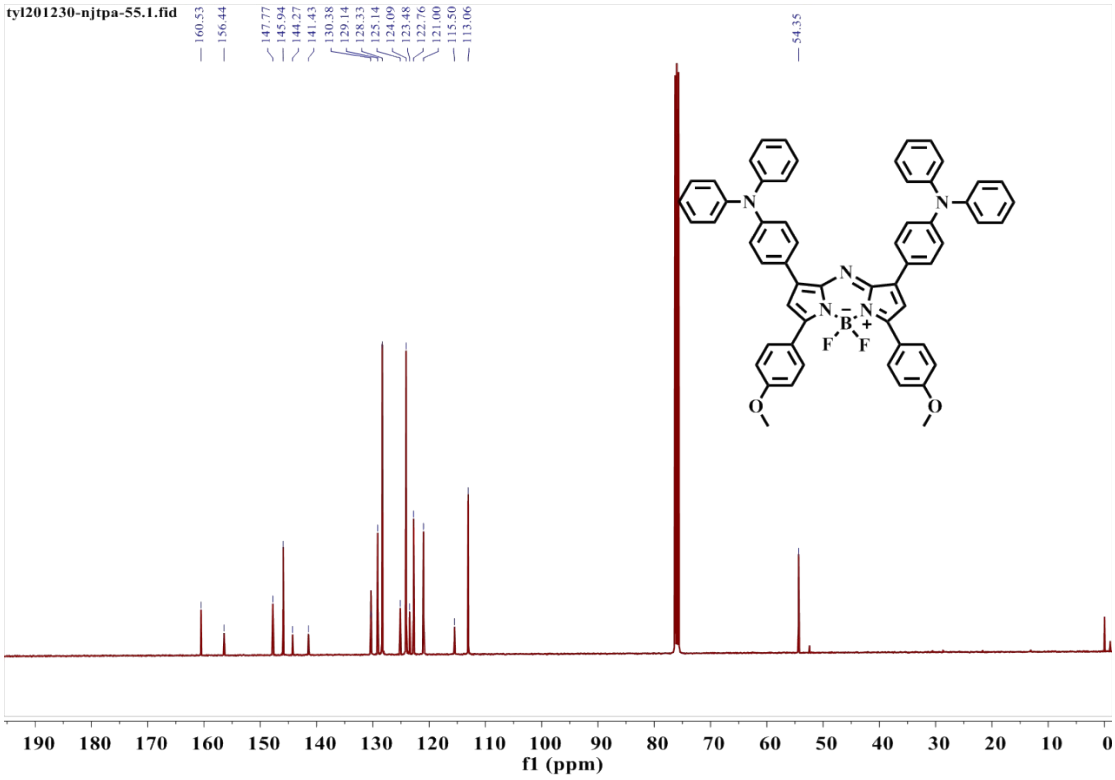

Figure S9. ^{13}C NMR spectrum of TAB in $CDCl_3$.

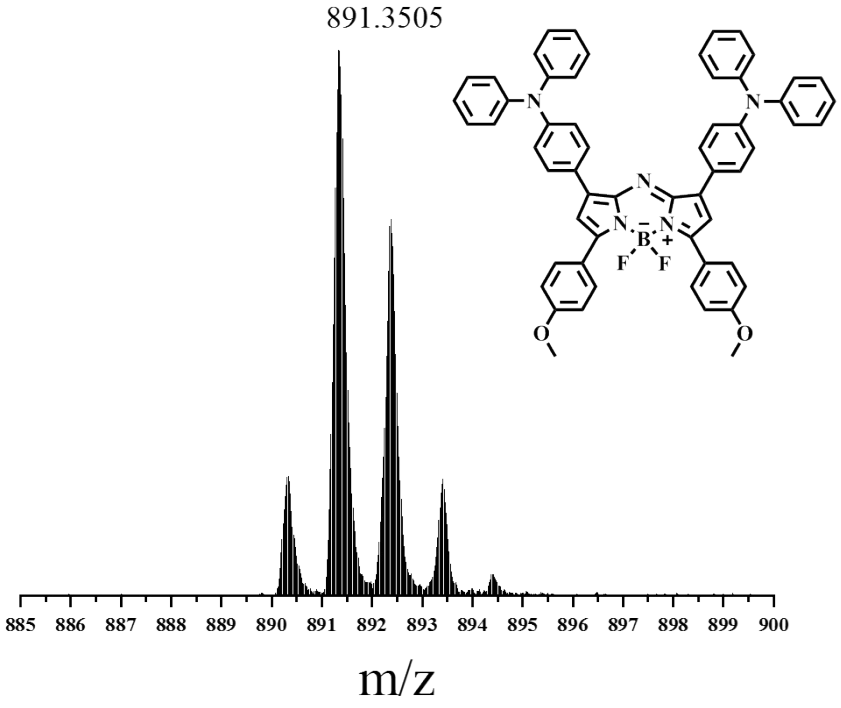

Figure S10. HRMS spectrum of TAB.

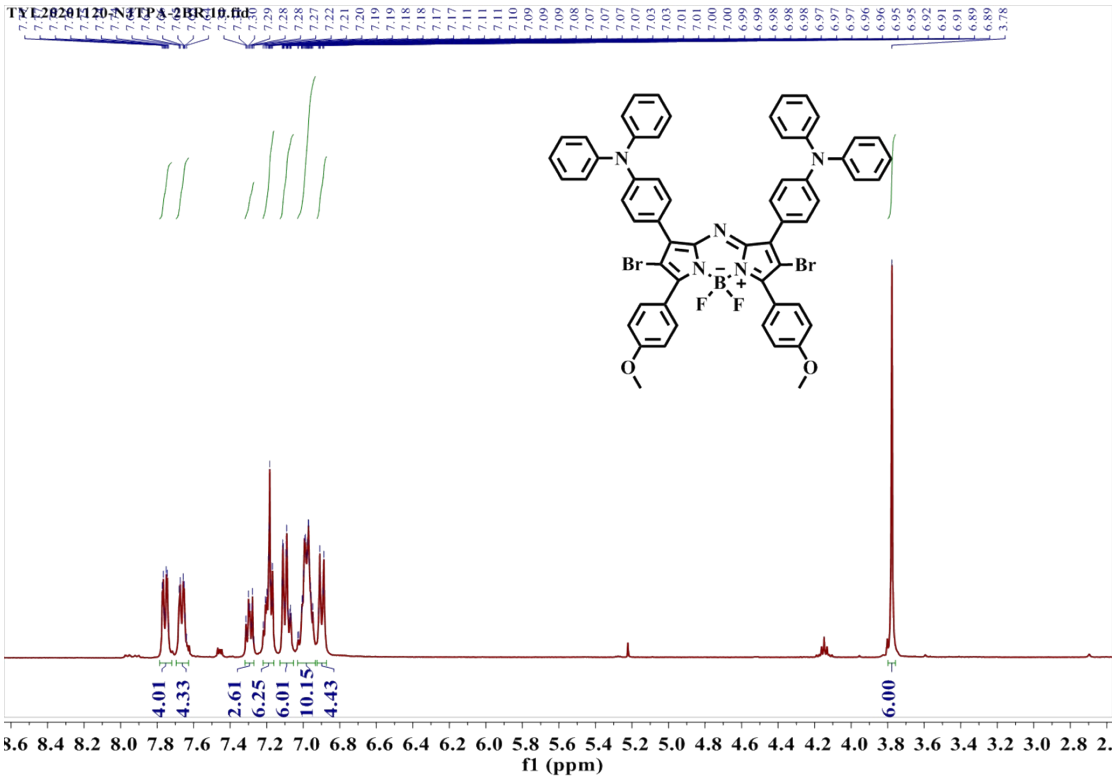

Figure S11. ^{1}H NMR spectrum of TAB-2Br in $CDCl_3$.

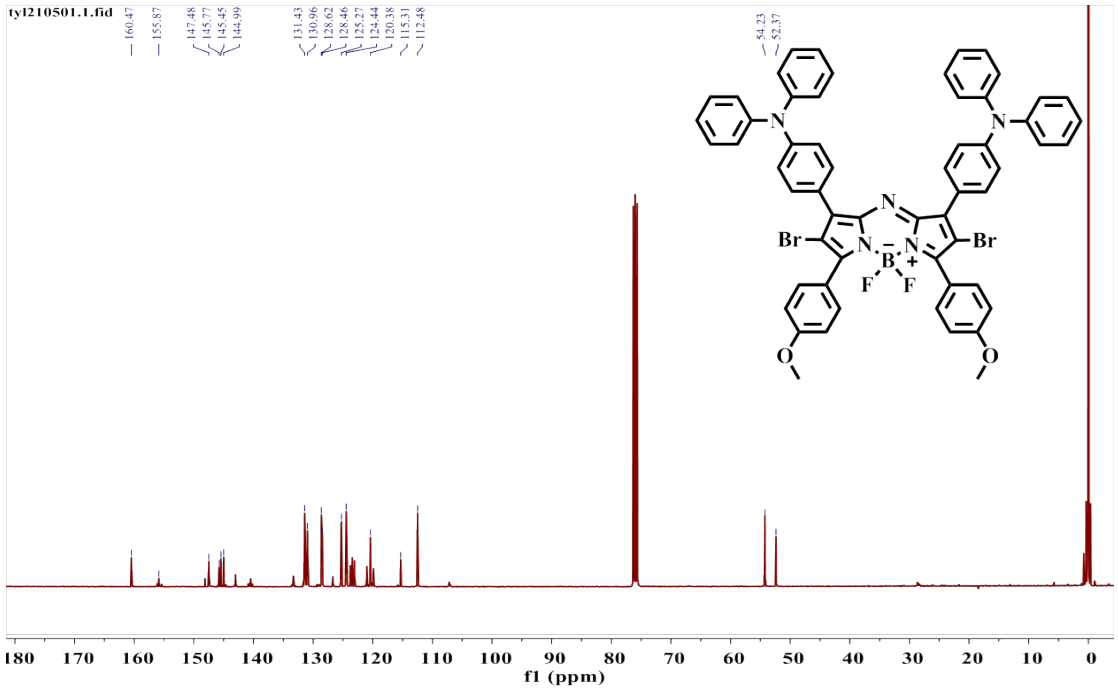

Figure S12. ^{13}C NMR spectrum of TAB-2Br in $CDCl_3$.

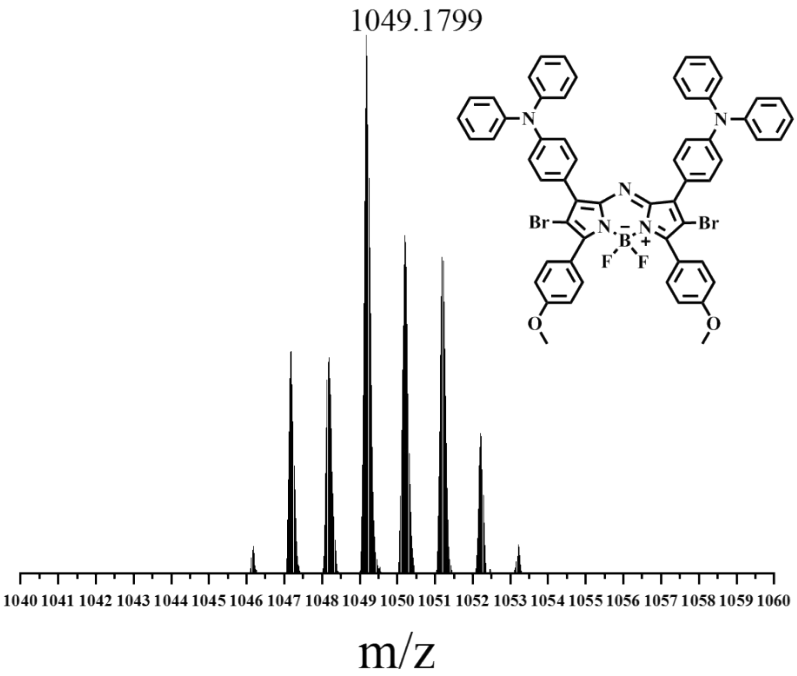

Figure S13. HRMS spectrum of TAB-2Br.

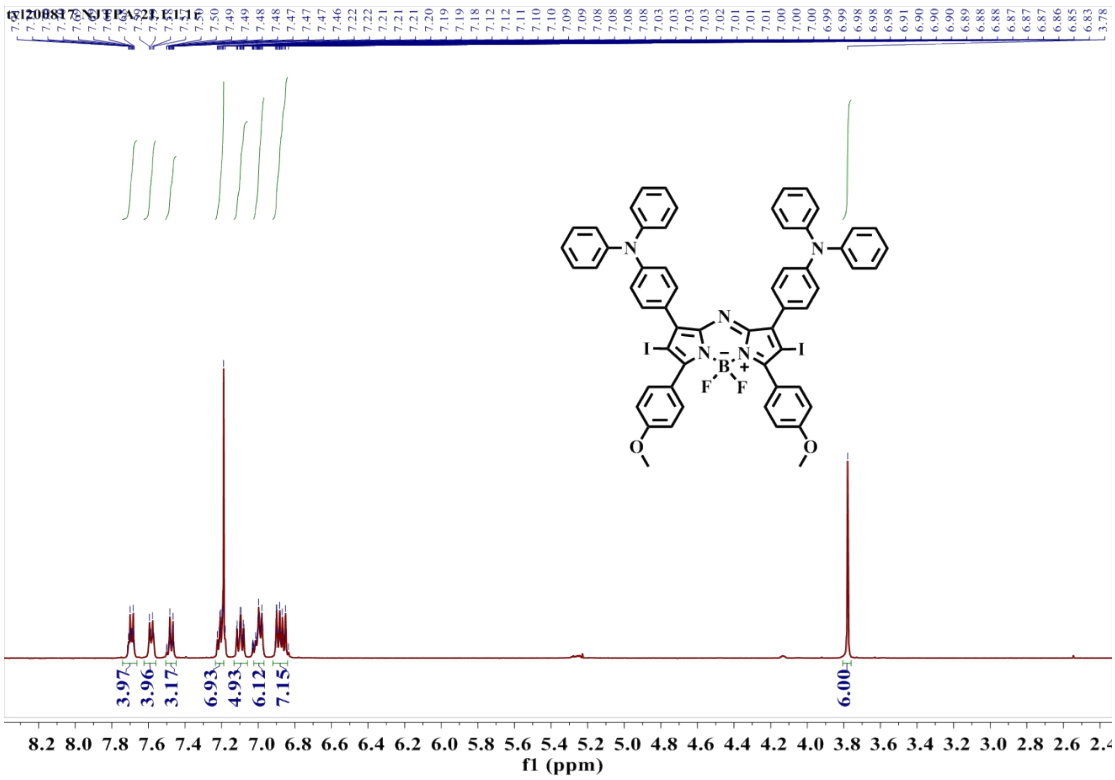

Figure S14. ^{1}H NMR spectrum of TAB-2I in $CDCl_3$.

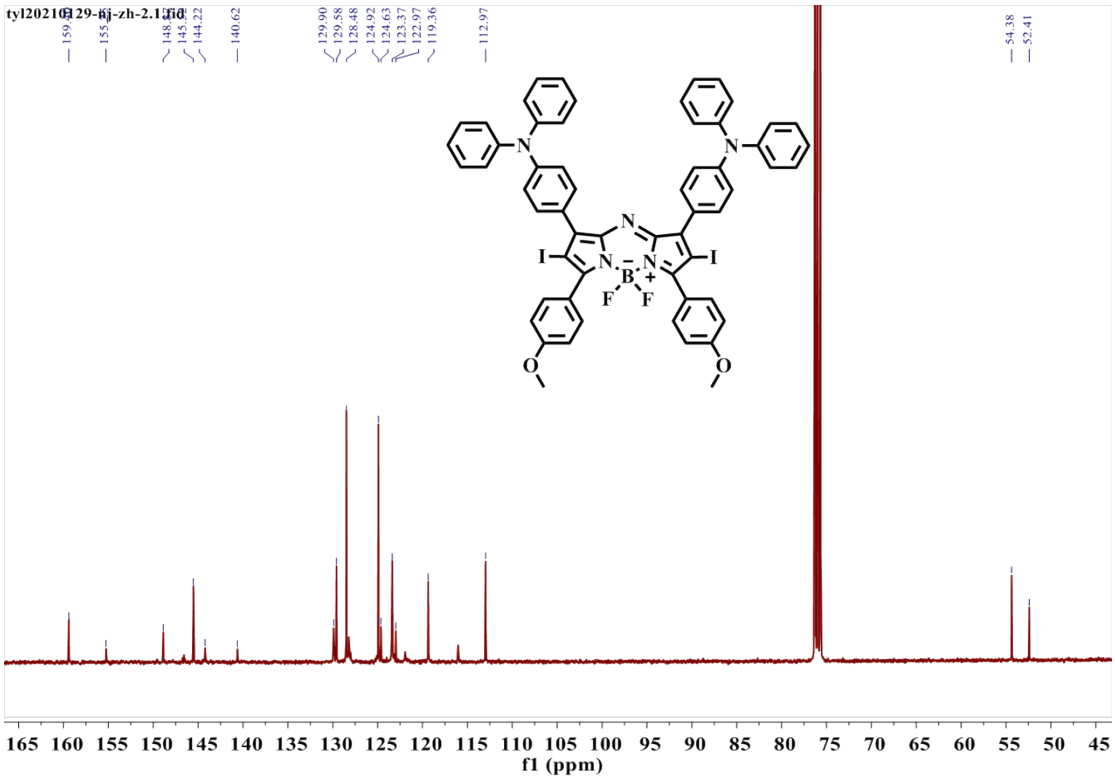

Figure S15. ^{13}C NMR spectrum of TAB-2I in $CDCl_3$.

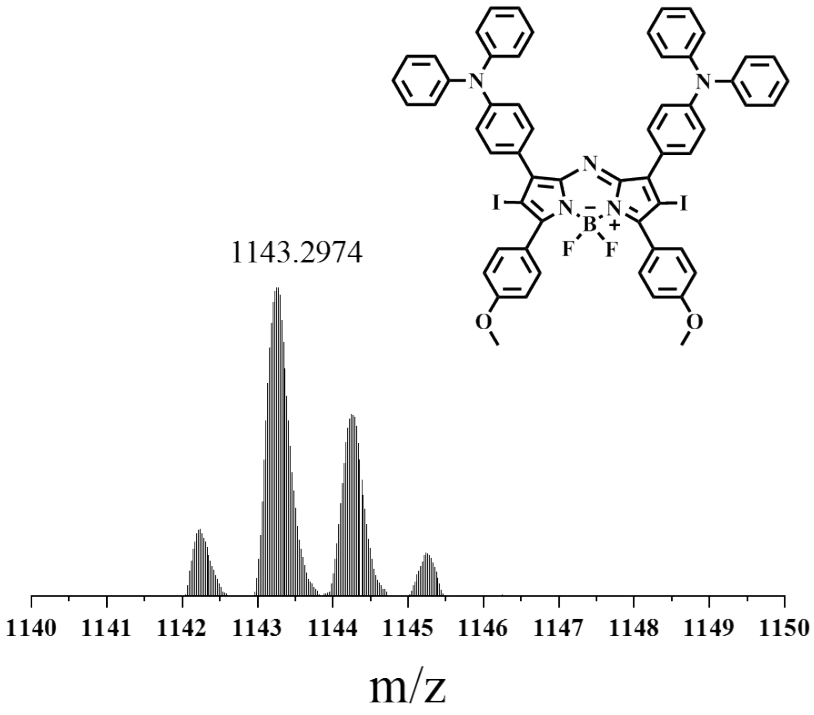

Figure S16. HRMS spectrum of TAB-2I.

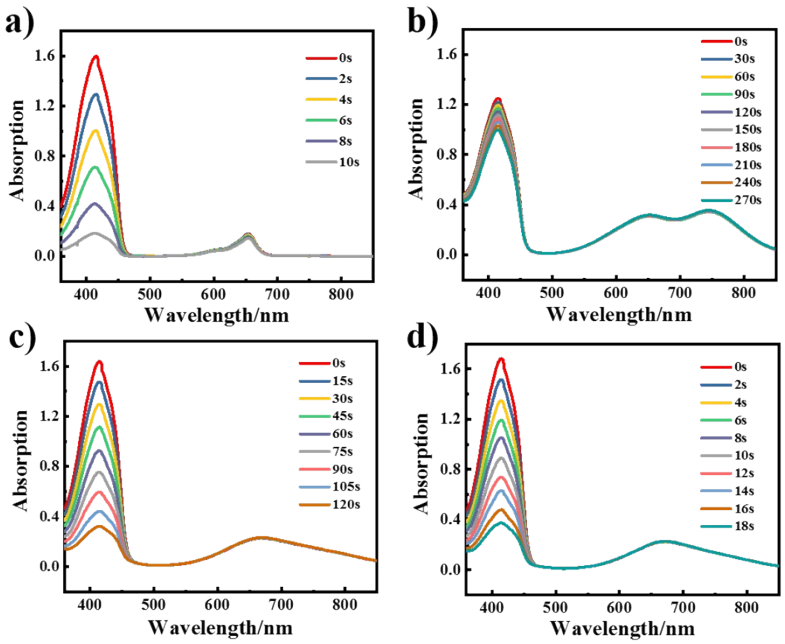

Figure S17. The absorption spectra changes of DPBF at 414 nm under 635 nm irradiation (25 mW) in DCM, a: MB, b: TAB, c: TAB-2Br, d: TAB-2I.

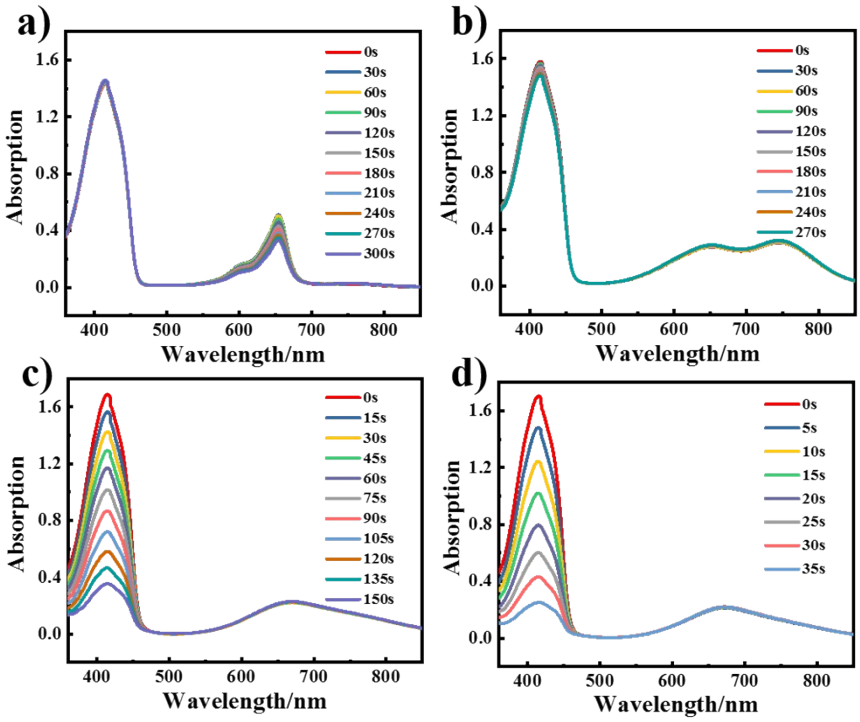

Figure S18. The absorption spectra changes of DPBF at 414 nm under 808 nm irradiation (25 mW) in DCM, a: MB, b: TAB, c: TAB-2Br, d: TAB-2I.

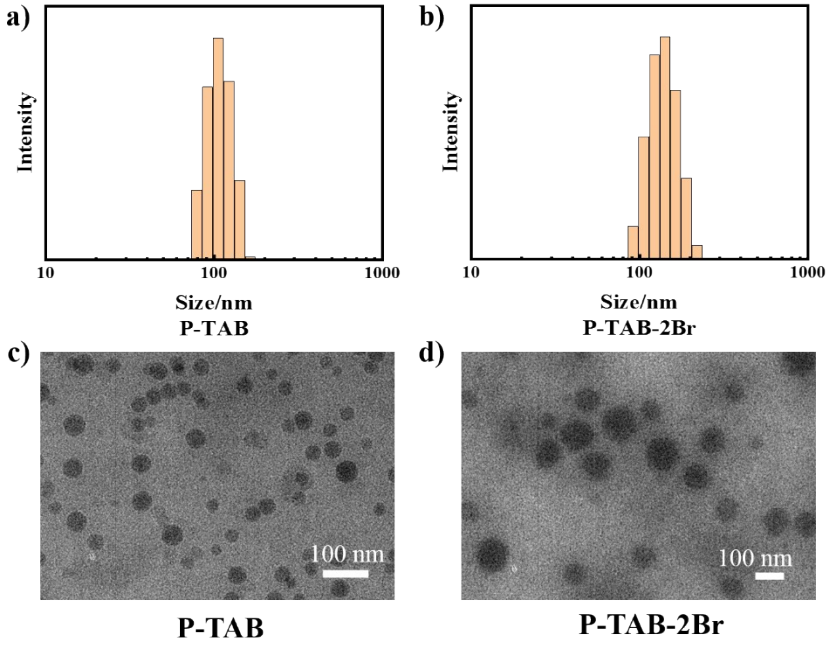

Figure S19. The DLS results and TEM images of P-TAB and P-TAB-2Br.

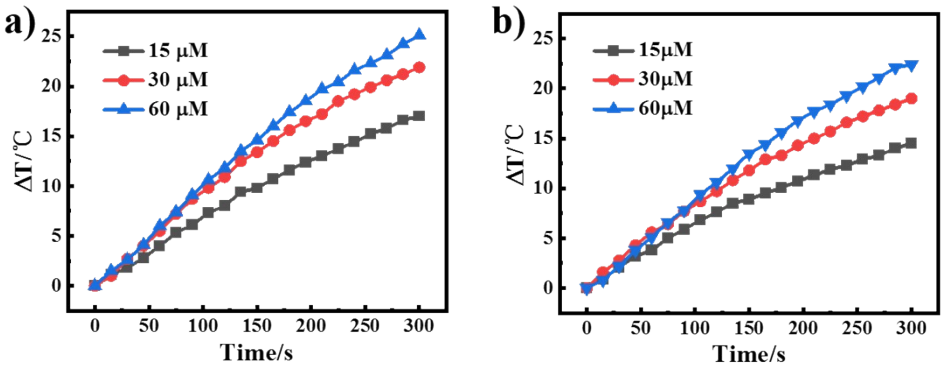

Figure S20. The temperature variation curves of different concentration P-TAB (a) and P-TAB-2Br (b) under 808 nm irradiation (0.8 W/cm^2).

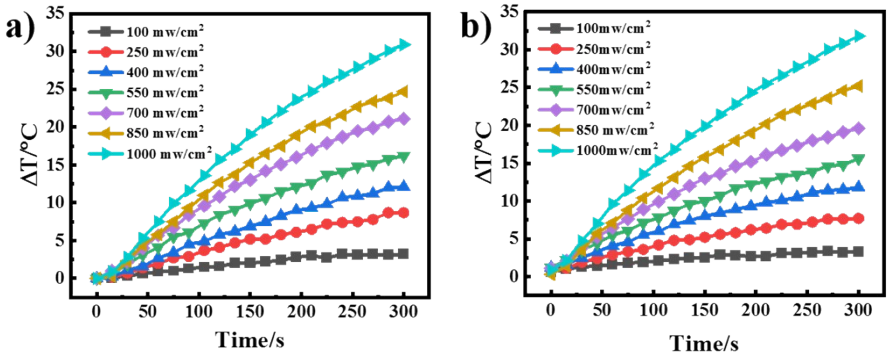

Figure S21. The temperature variation curves of P-TAB (a) and P-TAB-2Br (b) under different power 808 nm irradiation, concentration: 50 μM.

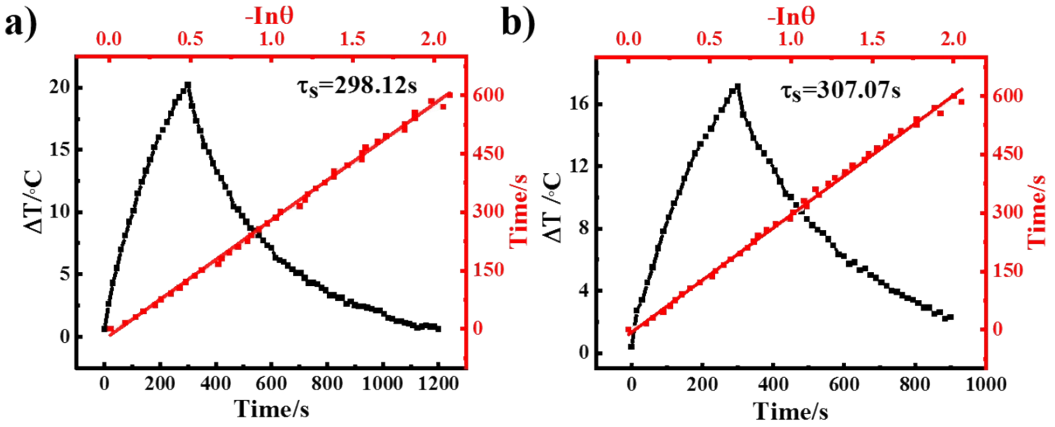

Figure S22.The photothermal conversion efficiency calculation of P-TAB (a) and P-TAB-2Br (b).

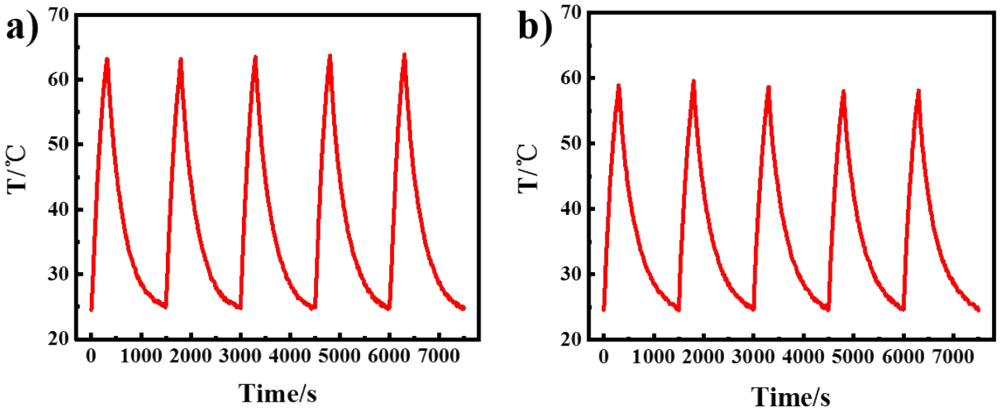

Figure S23. Photothermal stability study of P-TAB (a) and P-TAB-2Br (b) during five circles of heating-cooling processes.

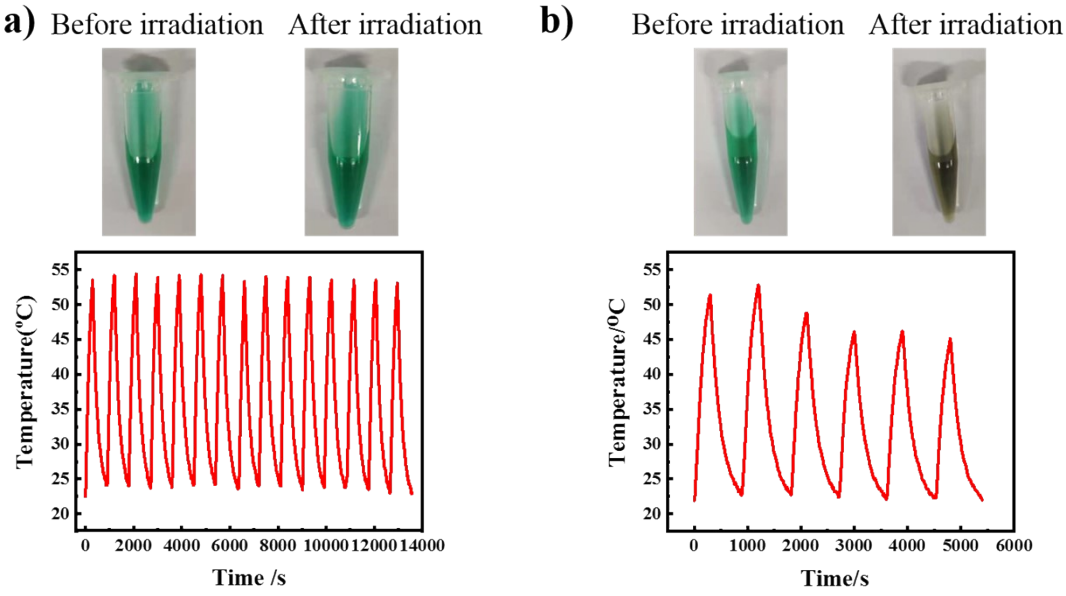

Figure 24. Digital photographs and photothermal cycle stability results of P-TAB-2I (50 μM) (a) and ICG (50 μM) (b), 808 nm irradiation, 1.25 W/cm^2.

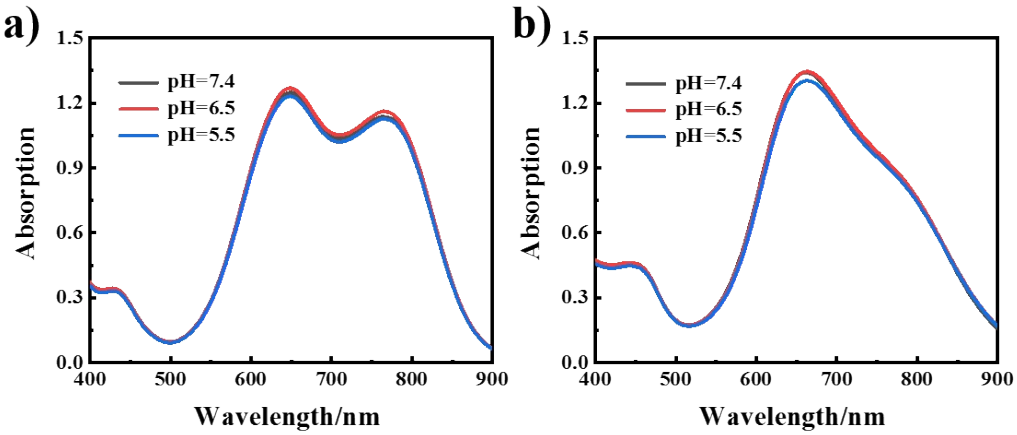

Figure S25. The absorption profiles of P-TAB (a) and P-TAB-2Br (b) in different pH conditions.

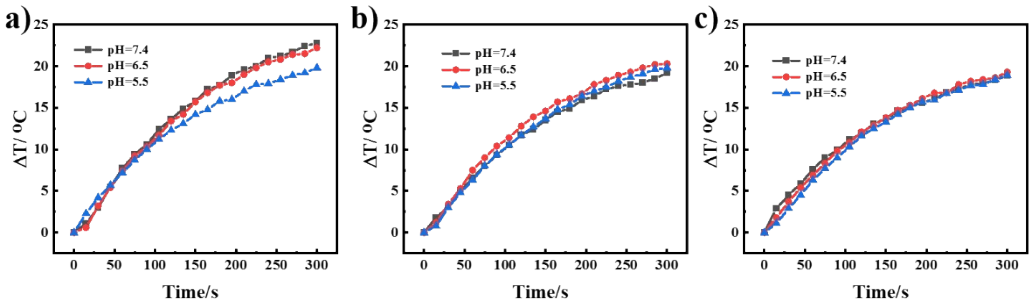

Figure S26. The temperature variation curves of P-TABs in different pH condition under power 808 nm irradiation (800 mW/cm^2), concentration: 40 μM.

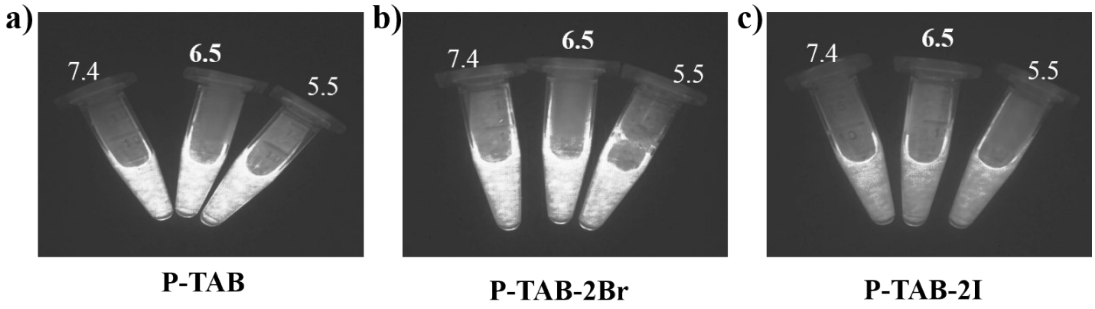

Figure S27. The fluorescence imaging of P-TABs in different pH condition under 808 nm irradiation (50 mW/cm^2), concentration: 40 μM.

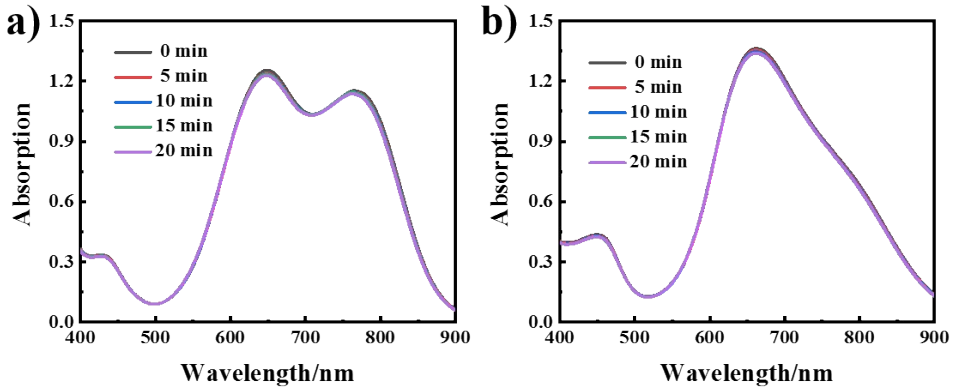

Figure S28. The absorption profiles of P-TAB (a) and P-TAB-2Br (b) after irradiation for a different time.

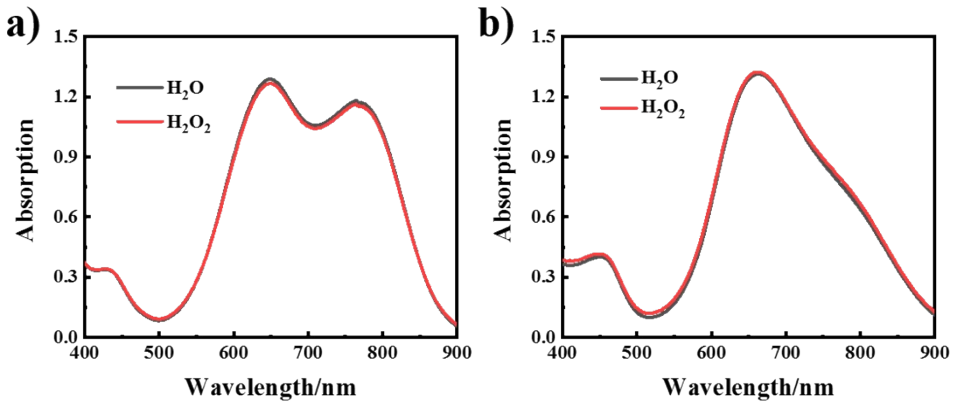

Figure S29. The resistance of P-TAB (a) and P-TAB-2Br (b) to H_2O_2 bleaching.

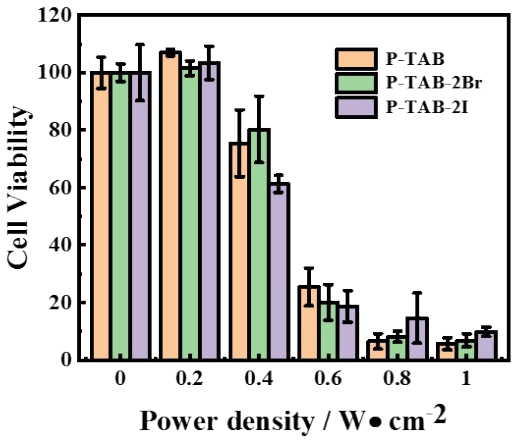

Figure S30. The MTT result of P-TABs (50 μM) on 4T1 cells under different 808 nm irradiation (mean ± SD, n = 4).

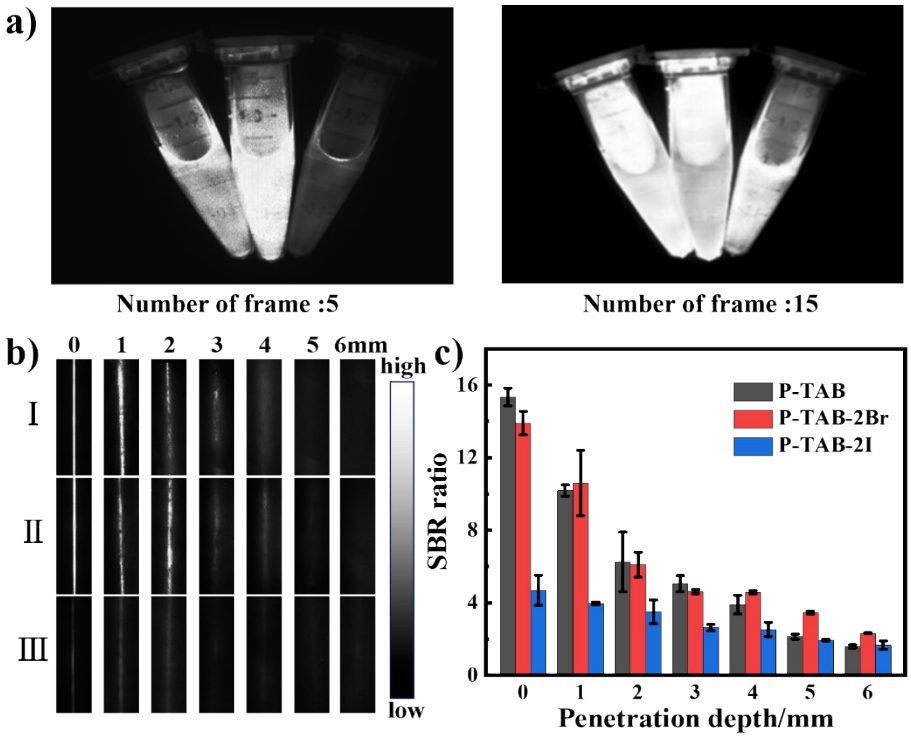

Figure S31. (a) The NIR-II fluorescence imaging photographs of P-TABs under 1000 nm long-wave pass filters. From left to right: P-TAB, P-TAB-2Br, and P-TAB-2I (with the same concentration: 100 μM). (b) The fluorescence imaging photographs of P-TABs under different thicknesses of chicken. I: P-TAB, II: P-TAB-2Br, III: P-TAB-2I. (Concentration: 100 μM). The number of the frame: 10. (c) SBR ratio of P-TABs at different depths.

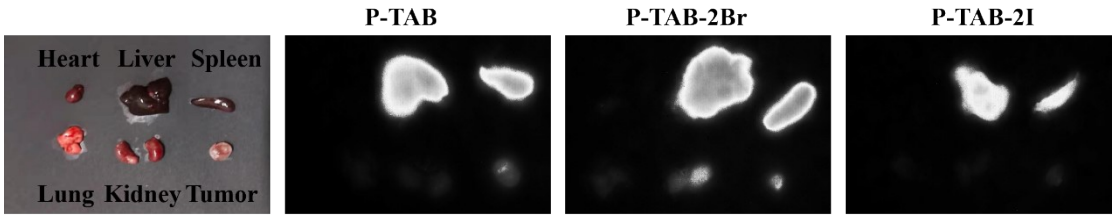

Figure S32. The *ex vivo* biodistribution of P-TABs NPs in main organs and tumor after 48 h post-injection under 808 nm laser excitation.

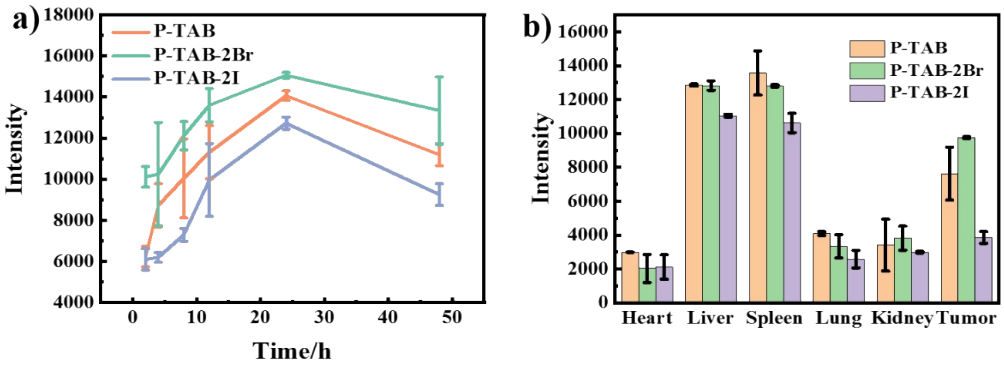

Figure S33. (a)The fluorescence intensity of the tumors at 2 h, 4 h, 8 h, 12 h, 24 h, and 48 h. (b) The fluorescence intensity in the main organs and tumor by average counts (n=2).

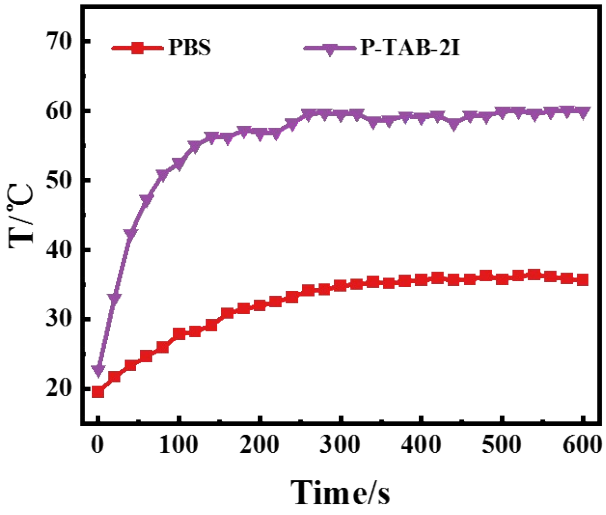

Figure S34. The temperature variation on the tumor during the irradiation process.

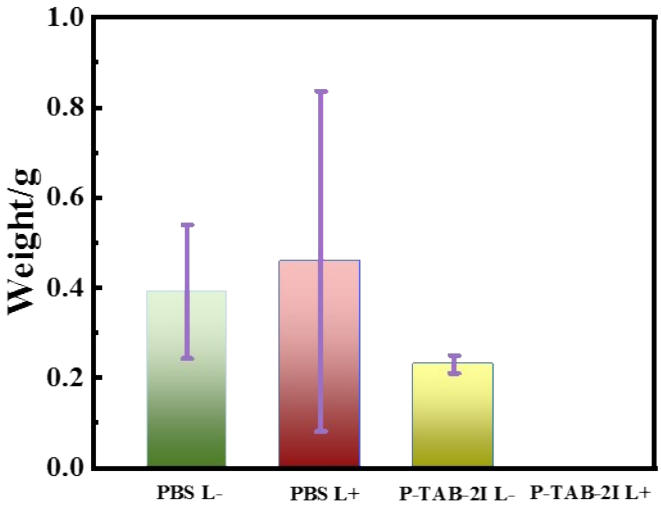

Figure S35. Tumors wet weight after 16 days treatment.

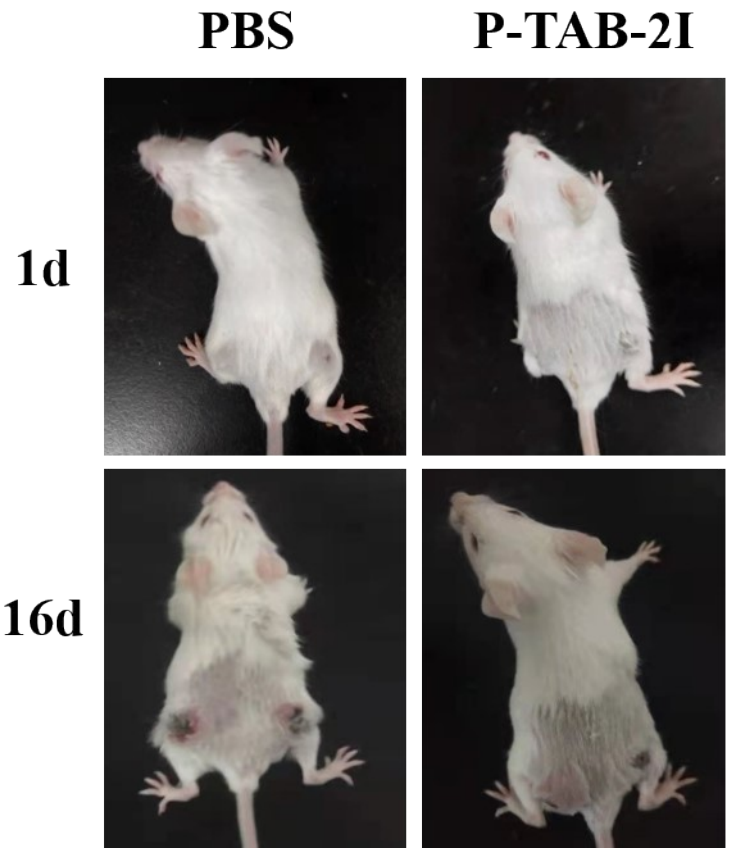

Figure S36. Digital images of different group mice at different time after treatment

References:

1. D. Xi, M. Xiao, J. Cao, L. Zhao, N. Xu, S. Long, J. Fan, K. Shao, W. Sun, X. Yan and X. Peng, *Adv. Mater.*, 2020, **32**, e1907855.